Journal of
Materials Chemistry C

ROYAL SOCIETY
OF CHEMISTRY

PAPER

View Article Online
View Journal

Check for updates

Cite this: DOI: 10.1039/d6tc00131a

Conformationally locked BODIPY donor–acceptor dyads: charge separation and recombination across a [2.2.2]bicyclooctane spacer

Metodej Dvoracek,[a] Yanran Wu,[b] Greta Sambucari,[c] Craig Newman,[a] Brendan Twamley,[d] Mathias O. Senge,[e] Jianzhang Zhao,*[b] Mariangela Di Donato*[cf] and Mikhail A. Filatov*[a]

Received 14th January 2026,
Accepted 4th April 2026

DOI: 10.1039/d6tc00131a

rsc.li/materials-c

Controlling the excited-state dynamics of charge-separated (CS) states in donor–acceptor (D–A) systems is challenging due to geometry changes from intramolecular rotations and vibrations. A key question is how molecular geometry governs the formation, stability, and recombination of CS states, and whether these processes can be decoupled from spin-related transitions such as intersystem crossing (ISC). Here, we investigate a rigid design strategy where BODIPY and anthracene chromophores are fused to a bicyclo[2.2.2]octane scaffold, fixing the D–A geometry and eliminating conformational flexibility. This setup enables direct evaluation of how geometric restriction affects charge-transfer dynamics. Femtosecond transient absorption spectroscopy shows efficient charge separation in polar solvents (2–9 ps), followed by rapid recombination (15–205 ps), with no detectable triplet state formation. Nanosecond transient absorption, 77 K luminescence, and singlet oxygen measurements confirm suppression of spin–orbit charge-transfer intersystem crossing (SOCT-ISC). These findings demonstrate that a rigid molecular architecture can block ISC but does not inherently extend CS state lifetimes. Our results provide new insight into the fate of CS states and emphasize that geometric rigidity alone does not ensure long-lived charge separation in D–A systems.

Introduction

Electron donor–acceptor (D–A) dyads are molecular systems in which an electron-donating unit (D) and an electron-accepting unit (A) are covalently linked within a single molecule and undergo directional electron transfer (ET) upon photoexcitation. Achieving rapid photoinduced charge separation while simultaneously suppressing charge recombination, thereby generating long-lived charge-separated (CS) states, has long been a central objective in the design of D–A dyads and has motivated decades of research.[1] This goal is inspired by natural photosynthetic systems, in which photoexcitation of (bacterio)-chlorophylls leads to directional electron transfer across a series of cofactors, resulting in a stabilized radical ion pair that persists long enough to drive multielectron redox processes.[2] Mimicking this strategy, artificial D–A systems aim to produce long-lived CS states that can power useful transformations such as water oxidation, proton reduction, or CO_2 fixation.[3] To achieve such functionality, researchers have systematically varied the spacer length and rigidity to control both the kinetics and thermodynamics of charge separation and recombination.

A ad range of molecular scaffolds have been developed to connect D and A units through various linkers (spacers), including flexible alkyl chains,[4] π-conjugated systems,[5] saturated cyclic systems[6] and polycyclic hydrocarbons (Fig. 1a).[7] The nature of the spacer, particularly its length, rigidity, and connectivity, defines the spatial arrangement of the donor and acceptor, including their separation, mutual orientation, and degree of conformational flexibility, all of which critically influence the efficiency of the ET process.[8] For instance, in systems where D and A are connected by rotatable σ-bonds, thermal motion can induce conformational changes that modulate orbital overlap and electronic coupling, complicating the interpretation of excited-state behaviour (Fig. 1b).[9]

---

[a] School of Chemical and Biopharmaceutical Sciences, Technological University Dublin, City Campus, Grangegorman, Dublin D07 ADY7, Ireland. E-mail: mikhail.filatov@tudublin.ie
[b] State Key Laboratory of Fine Chemicals, Frontiers Science Center for Smart Materials, School of Chemical Engineering, Dalian University of Technology, Dalian 116024, P. R. China. E-mail: zhaojzh@dlut.edu.cn
[c] LENS (European Laboratory for Non-Linear Spectroscopy), via N. Carrara 1, 50019 Sesto Fiorentino (FI) Firenze, Italy. E-mail: didonato@lens.unifi.it
[d] School of Chemistry, Trinity College Dublin, The University of Dublin, Dublin 2, Ireland
[e] Medicinal Chemistry, Trinity Translational Medicine Institute, St. James's Hospital, Trinity College Dublin, The University of Dublin, Dublin D08 W9RT, Ireland
[f] CNR-ICCOM, via M. del Piano 10, 50019 Sesto Fiorentino (FI), Italy

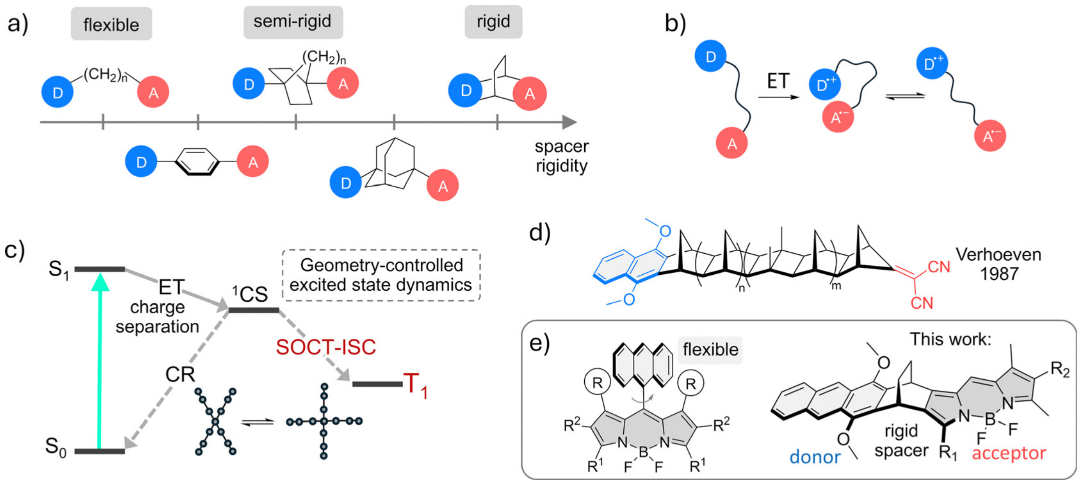

Fig. 1 Spacer rigidity and charge-transfer dynamics in donor–acceptor dyads. (a) Representative D–A dyads with flexible, semi-rigid, and rigid spacers. (b) Possible conformational changes in flexible dyads leading to different excited-state behaviours. (c) Simplified Jablonski diagram showing the interplay between charge separation, charge recombination and SOCT-ISC processes in flexible dyads. (d) Conformationally locked dyads based on rigid bicyclo[2.2.2]octane scaffolds studied by Verhoeven *et al.* (e) Previously studied *meso*-anthracenyl BODIPY vs rigid BODIPY–anthracene dyads studied in this work.

The use of rigid spacers allows restriction of molecular motion and decoupling of electronic processes from dynamic geometrical changes. In this context, "rigid" refers to molecular frameworks in which the change of the electronic structure and the reorganization of the adjacent solvent layers are not accompanied by any major modifications of their molecular geometry.[10]

Classic examples include norbornane,[11] adamantane,[12] triptycene,[13] and bicyclo[2.2.2]octane (BCO).[14] These saturated frameworks have demonstrated efficient electron[15] and energy[16] transfer, contradicting early assumptions that non-conjugated systems act as inert insulators and revealed that rigidity and σ-coupling can sustain strong electronic communication between the donor and acceptor units.

Some of these rigid dyads have achieved CT state lifetimes on the microsecond scale,[17] indicating that structural rigidity can indeed suppress recombination. However, formation of CS states is often followed by a recombination into a local triplet state (Fig. 1c), known as spin–orbit charge-transfer intersystem crossing (SOCT-ISC).[18] This process has attracted considerable attention in recent years as a mechanism for generating triplet states in heavy-atom-free organic dyes.[19] Efficient SOCT-ISC typically requires a near-orthogonal arrangement of donor and acceptor units, which enhances spin–orbit coupling through angular momentum changes during charge recombination.[20] Consequently, designing D–A systems with long-lived CS states involves a trade-off: while rigidifying the structure can extend CS lifetimes by suppressing structural relaxation, it may also promote SOCT-ISC by enforcing orthogonality, thereby accelerating recombination into the triplet state. This raises a question: can CS lifetimes be extended by introducing a rigid spacer that locks the system into a non-orthogonal geometry – one that disfavours SOCT-ISC? Testing this hypothesis requires access to conformationally locked dyads with a fixed, non-orthogonal configuration, which remain scarce due to the synthetic challenges associated with constructing such geometrically constrained architectures. In cases where the donor and acceptor are connected to cyclic frameworks through single C–C σ-bonds, torsional motion can persist even in conformationally constrained scaffolds such as adamantane or BCO. These motions persist in both ground and excited states, introducing uncertainty into geometry-dependent processes like SOCT-ISC. Furthermore, rigidity is frequently extrapolated from X-ray crystal structures, which do not necessarily reflect conformations in solution.

A few studies have attempted to address this gap by designing dyads in which both the donor and acceptor groups are fused to rigid polycyclic scaffolds. These fused systems eliminate internal rotational freedom and maintain a fixed mutual arrangement of the subunits. For example, the work of Verhoeven and co-workers[21] showed that such fused dyads (Fig. 1d) retained efficient charge separation, with electron transfer rates comparable to those of more flexible analogues. Interestingly, although triplet formation was suppressed, the CS state lifetimes were shorter (10–20 ns), attributed to enhanced radiative decay. A similar trend was reported by Chen *et al.*,[22] who observed fluorescence coming from CS states in rigid dyads with lifetimes of ∼9.7 ns. These findings challenge the assumption that rigidity prolongs lifetimes of CS states and suggest that radiative decay may dominate when non-radiative pathways, including vibrations and intersystem crossing, are inhibited.

To address these questions, we synthesized a new class of conformationally locked BODIPY–anthracene dyads in which the chromophores are rigidly fused to a bicyclo[2.2.2]octane scaffold. Previously reported BODIPY–anthracene dyads[23] with single C–C bond linkages have demonstrated efficient photoinduced charge transfer and SOCT-ISC, with triplet formation strongly dependent on molecular geometry: orthogonal arrangements yielded triplet quantum yields near unity and lifetimes exceeding 100 μs, whereas systems deviating from orthogonality showed significantly reduced triplet formation. In contrast, a rigid architecture enforces a fixed, non-orthogonal geometry and eliminates conformational flexibility – features not accessible in previously studied *meso*-substituted BODIPY dyads. These new systems provide rare, structurally defined models to investigate how rigid, non-orthogonal arrangements affect charge-transfer and intersystem crossing dynamics. Femtosecond transient absorption spectroscopy revealed fast charge separation but unexpectedly short-lived charge-transfer states, with no evidence for SOCT-ISC. These results confirm that SOCT-ISC is suppressed in a rigid, non-orthogonal dyad, which can be used to decouple charge separation from triplet formation, offering a new strategy for modulating excited-state dynamics in molecular D–A systems. By establishing clear links between geometry, rigidity, and recombination pathways, this work advances the fundamental understanding of photoinduced processes in donor–acceptor systems and opens new directions for the rational design of fluorophores and molecular photonic devices.

Results and discussion

Molecular design and synthesis

Reported BODIPY-based electron donor–acceptor dyads commonly feature aromatic donors such as anthracene attached at the *meso*-,[23b,24] 3,5-,[25] or 2,6-positions[26] of the BODIPY core. These substitution patterns predominate due to the availability of well-established synthetic methods and the commercial or synthetic accessibility of suitable precursors. However, analysis of X-ray crystal structures for such systems reveals that the dihedral angle between the BODIPY π-plane and the *meso*-aryl group typically ranges from 70° to 90°, reflecting partial rotational freedom around the C_{meso}–C_{Aryl} bond.[23b,24] This flexibility is influenced by the substitution pattern on the BODIPY core: different substituents, particularly on the pyrrolic rings, can modulate steric interactions and thus alter the rotation barrier. To eliminate this conformational flexibility, we designed a series of rigid dyads in which the donor (1,4-dimethoxyanthracene) and acceptor (BODIPY) units are fused to a bicyclo[2.2.2]octane spacer. As can be seen from the reported structure containing this scaffold, it enforces a fixed geometry between the chromophores, minimizing torsional freedom and ensuring a well-defined spatial arrangement.[27] The synthetic strategy builds on our previously reported approach to asymmetrically substituted BODIPYs.[28] The bicyclic system is introduced at an early stage *via* the Diels–Alder reaction of anthracene-1,4-dione with 1,3-cyclohexadiene, forming a rigid bicyclo[2.2.2]octene scaffold. This compound was then converted into the key anthracene–pyrrole precursor **PA-1** (Scheme 1) by following a previously published approach.[29] The ethoxycarbonyl group in **PA-1** was selectively reduced using $LiAlH_4$ to give **PA-2**, thereby removing the carbonyl functionality, which is known to influence BODIPY excited-state dynamics in related structures.[30] Subsequent formylation of **PA-1** and **PA-2** *via* a Vilsmeier reaction afforded **FPA-1** and **FPA-2** in high yields and with good regioselectivity. Condensation of these aldehydes with 2,4-dimethylpyrrole or 3-ethyl-2,4-dimethylpyrrole, followed by complexation with $BF_3·Et_2O$, provided the target BODIPY dyads **DMA-BDPs 1–4**. The choice of the pyrrole component was guided by the need to modulate the redox properties of the BODIPY core: alkyl substitution at the 1- and 7-positions is known to shift the reduction potential by ∼0.05–0.1 eV, enabling fine-tuning of the driving force for charge transfer. The condensation reactions between formylpyrroles and pyrroles yielded the target BODIPY dyads in good yields (12–50%).

Reference compounds **BDP-1** and **BDP-2** were prepared to support the interpretation of the photophysical behavior of the dyads. These compounds share the same BODIPY chromophore

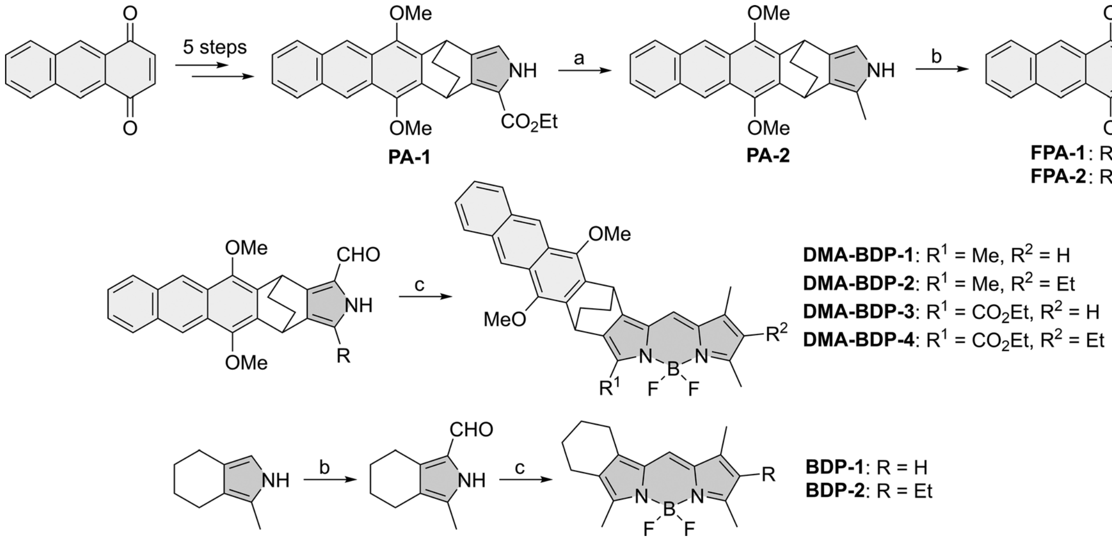

Scheme 1 Synthesis of BODIPY–anthracene dyads and reference compounds. (a) $LiAlH_4$, THF, reflux (58%); (b) (i) $POCl_3$, DMF, DCE; (ii) KOAc, H_2O, reflux (**FPA-1**: 84%, **FPA-2**: 93%); (c) (i) 2,4-dimethylpyrrole or 3-ethyl-2,4-dimethylpyrrole, $POCl_3$, DCM, r.t.; (ii) $BF_3·Et_2O$, DIPEA, DCM, r.t. (**DMA-BDP-1**: 49%, **DMA-BDP-2**: 50%, **DMA-BDP-3**: 12%, **DMA-BDP-4**: 34%, **BDP-1**: 82%, **BDP-2**: 22%).

structure, including the annelated cyclohexane ring on one of the pyrrolic units, but lack the anthracene moiety and therefore do not undergo intramolecular charge transfer. Synthesized compounds were obtained in analytically pure form, as confirmed by NMR spectroscopy and high-resolution mass spectrometry (HRMS, SI).

X-Ray crystallography

To gain information about structural features of the synthesized compounds, crystal structures of **PA-1** and **DMA-BDP-4** were obtained *via* single crystal X-ray diffraction crystallography (Fig. 2), see details in the SI, page S24.[31] The **DMA-BDP-4** crystal structure reveals a BODIPY core root mean square distance (RMSD) of 0.040 Å and an anthracene core RMSD of 0.048 Å, while **PA-1** exhibits a higher anthracene RMSD of 0.086 Å, indicating higher structural flexibility in the pyrrolic structure, prior to BODIPY formation. Okujima *et al.* reported a BODIPY dye bearing bicyclo[2.2.2]octane units[27] (CSD entry SUTKAU, Fig. S29), which shows a BODIPY core RMSD of 0.043 Å, marginally less planar than that of **DMA-BDP-4**. A further comparison of **DMA-BDP-4** can be made to a reference compound from our previous work:[32] **aBDP-1** (Fig. 2c). **aBDP-1** is considerably more planar at the BODIPY core, with an RMSD value of only 0.012 Å.

In **DMA-BDP-4**, the torsion angle between the mean planes of the BODIPY and anthracene units is 13.109(4)°. The geometry of the bicyclo[2.2.2]octane fragment remains relatively unchanged between the BODIPY and the pyrrole; the **DMA-BDP-4** spacer group exhibits external (α) and internal (β) angles of 106.420(2)° and 106.3127(15)° (Fig. 2b), while **PA-1** exhibits 104.960(3)° and 106.7620(17)°, respectively. These bicyclo[2.2.2]octane spacer group angles are very similar to those observed in SUTKAU, with α and β angles of 106.733° and 106.231°, respectively. Due to the minimal change in the rigid spacer group geometry, and therefore the alignment of the anthracene fragment with respect to the BODIPY core, it can be seen that the spacer plays a role in the rigid arrangement of the donor and acceptor groups.

A comparison between the crystallographically determined structure and the DFT-optimized geometry, determined with Gaussian 16[33] (Table S3, SI), reveals a high degree of agreement, both in bond lengths and in the overall molecular geometry. Key parameters such as the α and β angles of the bicyclo[2.2.2]octane spacer, RMSD values of the BODIPY and anthracene cores, and dihedral angles between the subunits show minimal deviation between the optimized and solid-state structures. These findings confirm the high conformational rigidity of the molecule, as the spatial arrangement of the donor and acceptor units remains essentially unchanged upon crystallization.

Electrochemical studies

The redox properties of the compounds were investigated using cyclic voltammetry (Fig. S12). For **BDP-1**, a reversible reduction wave was observed at −1.65 V (*vs.* Fc/Fc$^+$), along with a reversible oxidation wave at +0.64 V (*vs.* Fc/Fc$^+$). For **BDP-2**, both redox events were irreversible: a reduction peak at −1.96 V and an oxidation peak at +0.44 V (*vs.* Fc/Fc$^+$). These values are closely aligned with those reported for parent BODIPY dyes lacking the peripheral six-membered ring.[34] The redox behaviour of **DMA-BDP-1** was characterized by an irreversible reduction at −1.63 V and an irreversible oxidation at +0.59 V (Fig. 5c). **DMA-BDP-2** displayed similar electrochemical features (Table 1), indicating comparable electronic properties between the two dyads.

The Gibbs free energy changes (ΔG_{CS}) associated with photoinduced charge separation were estimated using the Rehm–Weller equation.[35] As shown in Table 1, in non-polar solvents such as *n*-hexane (HEX) and toluene (TOL), ΔG_{CS} values are positive, indicating thermodynamically unfavourable charge separation. In contrast, in polar solvents like dichloromethane (DCM) and acetonitrile (ACN), ΔG_{CS} becomes negative, suggesting that intramolecular charge transfer is thermodynamically allowed.

These results are consistent with the steady-state fluorescence data (Fig. 3), which show strong quenching of emission for **DMA-BDP-1** and **DMA-BDP-2** in polar solvents, while fluorescence is retained in non-polar media.

We also estimated the energy of the CS state for **DMA-BDP-1** and **DMA-BDP-2** in various solvents. As expected, the CS state energy strongly depends on solvent polarity, in agreement with previous reports.[18] However, in all cases, the CS state energy remains higher than that of the localized triplet excited state (^{3}LE) of the BODIPY chromophore. This indicates that the lowest excited state is the ^{3}LE state rather than the CS state. Based on the empirical relationship between oxidation potential and the HOMO energy level, HOMO $\approx -(E_{\mathrm{Ox}} + 4.8)$ eV, we estimated the frontier orbital energies from the experimental electrochemical data. The resulting values are in good agreement with those obtained from DFT calculations (Fig. S33).

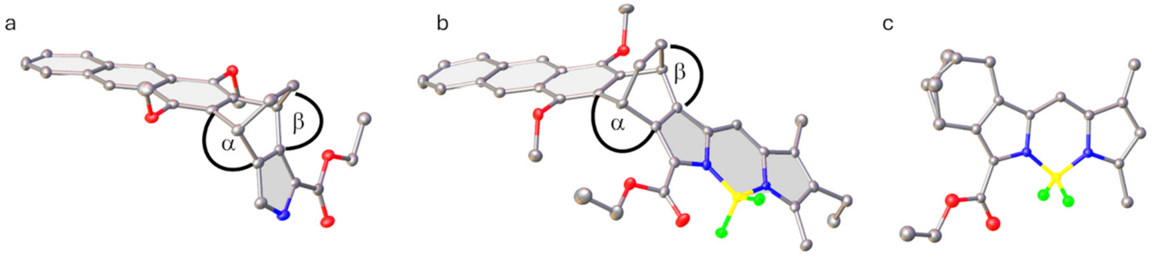

Fig. 2 Single-crystal X-ray crystallographic structures: (a) **PA-1**, highlighting the rigid spacer group angles α and β, (b) **DMA-BAD-4** and (c) reference compound **aBDP-1** with atomic displacement shown at 50% probability. The methanol solvate in **DMA-BDP-4** and all hydrogen atoms are omitted for clarity.

Table 1 Oxidation (E_{Ox}) and reduction (E_{Red}) potentials, Gibbs free energy change for charge separation (ΔG_{CS}), and energy of the charge-separated states (E_{CS}) for the studied compounds in various solvents[a]

			ΔG_{CS} (eV)/E_{CS} (eV)			
Compound	E_{Ox}/V	E_{Red}/V	HEX	TOL	DCM	ACN
BDP-1	+0.64	−1.65	—	—	—	—
BDP-2	+0.44	−1.96	—	—	—	—
DMA-BDP-1	+0.59	−1.63	+0.33/2.69	+0.16/2.51	−0.34/2.02	−0.49/1.89
DMA-BDP-2	+0.72	−1.52	+0.16/2.48	+0.06/2.36	−0.27/2.04	−0.38/1.96
DMA-BDP-3	+0.68, +0.80	−1.29	−0.24/2.14	−0.34/2.04	−0.63/1.77	−0.74/1.69
DMA-BDP-4	+0.66, +0.80	−1.36	−0.15/2.18	−0.24/2.09	−0.52/1.83	−0.62/1.76

[a] Cyclic voltammetry was performed in N_2-saturated dichloromethane containing 0.10 M Bu_4NPF_6 as the supporting electrolyte. A platinum wire was used as the counter electrode, a glassy carbon electrode as the working electrode, and an Ag/$AgNO_3$ electrode as the reference. Ferrocene (Fc) was added as an internal standard, and its oxidation peak was set to 0 V. E_{00} values correspond to the estimated singlet excited-state energy, determined from the intersection of normalized absorption and fluorescence spectra. HEX = hexane, TOL = toluene, DCM = dichloromethane, and ACN = acetonitrile.

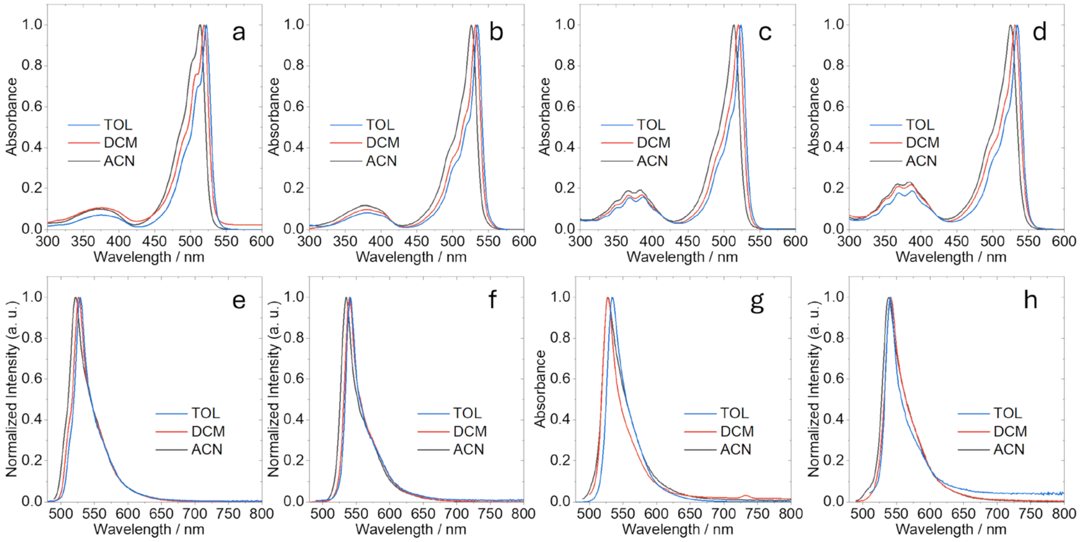

Fig. 3 Absorption spectra of (a) **BDP1**, (b) **BDP2**, (c) **DMA-BDP1**, and (d) **DMA-BDP2** in toluene (TOL), dichloromethane (DCM) and acetonitrile (ACN). The normalized fluorescence emission spectra of (e) **BDP1**, (f) **BDP2**, (g) **DMA-BDP1** and (h) **DMA-BDP2** in TOL, DCM and ACN.

The ester-substituted dyads **DMA-BDP-3** and **DMA-BDP-4** display noticeably different electrochemical behaviour (Fig. S14). Both compounds show two oxidation processes, with oxidation potentials at +0.68 and +0.80 V for **DMA-BDP-3** and +0.66 and +0.80 V for **DMA-BDP-4**, together with reduction waves at −1.29 and −1.36 V, respectively (Table 1). The substantially less negative reduction potentials of these dyads indicate that incorporation of the ester groups significantly increases the electron-accepting ability of the BODIPY unit. As a result, charge separation becomes thermodynamically favourable already in non-polar solvents: the calculated ΔG_{CS} values are negative in all media investigated, from *n*-hexane to acetonitrile. Consistent with this, the estimated CS-state energies are markedly lower and decrease from 2.14 and 2.18 eV in *n*-hexane to 1.69 and 1.76 eV in acetonitrile, respectively. Thus, ester substitution strongly stabilizes the charge-separated state and shifts the electron-transfer equilibrium towards charge separation even in weakly polar environments.

Optical properties

Detailed photophysical investigations were carried out for **DMA-BDP-1** and **DMA-BDP-2**, together with their reference compounds **BDP-1** and **BDP-2** as the most suitable systems for isolating the effect of rigid geometry on charge separation and intersystem crossing. The ethoxycarbonyl-substituted dyads **DMA-BDP-3** and **DMA-BDP-4** were excluded because the corresponding parent BODIPYs (lacking the anthracene group) already exhibit an intrinsic ISC pathway. In our previous work,[28] we showed that triplet formation in mono-ethoxycarbonyl-substituted BODIPYs arises from a reduced singlet–triplet energy gap and population of triplet states proceeds *via* an $S_1 \rightarrow T_2$ pathway. Therefore, in **DMA-BDP-3** and **DMA-BDP-4**, any triplet population cannot be assigned unambiguously to SOCT-ISC or another ISC pathway. Basic photophysical data for **DMA-BDP-3** and **DMA-BDP-4** are provided in the SI (Fig. S10).

The absorption spectra of **DMA-BDP-1** and **DMA-BDP-2** (Fig. 3) closely resemble the superposition of the spectra of

Table 2 Steady-state optical properties of **BDP-1**, **BDP-2**, **DMA-BDP-1** and **DMA-BDP-2** in cyclohexane CYH), toluene (TOL), dichloromethane (DCM), ethyl acetate (EA) and acetonitrile (ACN)

Compound	Solvent (ε_r)[a]	λ_{abs} (nm)	λ_{em} (nm)	Lifetime τ_1, τ_2 (%)	$\Delta\lambda$ (nm)	Φ_{Fl}[b]	Φ_Δ[c]
BDP-1	CYH (2.0)	521	526	4.9 (100)	5	0.82	—
	TOL (2.4)	522	529	4.5 (100)	7	0.81	—
	EA (6.0)	515	521	5.1 (100)	6	0.92	—
	DCM (8.9)	519	526	5.1 (100)	7	0.77	—
	ACN (37.5)	513	522	5.7 (100)	9	0.79	—
BDP-2	CYH (2.0)	533	538	5.3 (100)	5	0.72	—
	TOL (2.4)	535	541	4.7 (100)	6	0.65	—
	EA (6.0)	528	535	5.5 (100)	7	0.82	—
	DCM (8.9)	532	540	5.5 (100)	8	0.67	—
	ACN (37.5)	526	535	5.8 (100)	9	0.63	—
DMA-BDP-1	CYH (2.0)	522	530	2.4 (47), 4.5 (53)	8	0.95	0.075
	TOL (2.4)	524	534	1.2 (5), 4.3 (95)	10	0.91	0.07
	EA (6.0)	516	529	0.4 (66), 5.1 (34)	13	0.02	0.05
	DCM (8.9)	520	528	0.1 (15), 4.9 (85)	8	0.02	0.03
	ACN (37.5)	514	524	0.3 (8), 4.7 (92)	10	0.01	<0.01
DMA-BDP-2	CYH (2.0)	533	540	2.4 (41), 4.9 (59)	7	0.96	0.06
	TOL (2.4)	534	543	1.1 (5.1), 4.4 (95)	9	0.89	0.06
	EA (6.0)	527	537	1.9 (39), 3 (61)	10	0.37	0.09
	DCM (8.9)	531	540	0.2 (41), 5 (59)	9	0.03	0.03
	ACN (37.5)	525	537	0.4 (10), 5.4 (90)	12	0.01	<0.01

[a] Dielectric constant. [b] Fluorescence quantum yields were measured using rhodamine 6G as a standard (Φ_{Fl} = 0.95 in EtOH).[36] [c] Measured using 1,9-dimethylanthracene as a singlet oxygen sensor and 2,6-diiodo-8-phenyl-BODIPY as a reference photosensitizer (Φ_Δ = 0.85 in toluene).[37]

the parent BODIPY chromophore and 1,4-dimethoxyanthracene, indicating the absence of significant ground-state electronic coupling between donor and acceptor moieties. No new absorption bands attributable to a direct $S_0 \rightarrow {}^1CS$ (charge transfer absorption) transition were observed for any of the dyads.

Both DMA-BDP and BDP reference compounds show modest negative solvatochromism in their absorption spectra, with the absorption maxima of **DMA-BDP-1** and **DMA-BDP-2** blue-shifting by 6 nm and 8 nm, respectively, when moving from nonpolar cyclohexane to polar acetonitrile. This shift, although less pronounced than in previously reported unsymmetrical BODIPY systems,[28] suggests a decrease in dipole moment upon excitation, consistent with negative solvatochromism. This trend is also reflected in the emission spectra, which display minimal changes in Stokes shift across the solvent series (Fig. 3e–h). A marked solvent-dependent quenching of fluorescence is observed for **DMA-BDP-1** and **DMA-BDP-2**. For **DMA-BDP-1**, the fluorescence quantum yield drops from 0.95 in cyclohexane to 0.006 in acetonitrile (Table 2). In contrast, the reference compounds **BDP-1** and **BDP-2** retain high fluorescence quantum yields across all solvents.

Unlike *meso*-anthracenyl substituted BODIPY derivatives, where red-shifted, broad emission bands have been previously attributed to emission from the CS state to the ground state,[38] no such CT-related emission features were observed here. Comparison of **DMA-BDP-1** and **DMA-BDP-2**, which differ in the substitution pattern at the pyrrolic ring, shows that introducing additional alkyl groups results in a slight red shift (~10 nm) in emission.

Notably, **DMA-BDP-2** retains a higher fluorescence quantum yield in polar solvents compared to **DMA-BDP-1**, suggesting that increased alkylation reduces the driving force of the photoinduced charge separation, which aligns with earlier observations for related BODIPY derivatives.[39] Fluorescence lifetime measurements reveal monoexponential decays for **BDP-1** and **BDP-2**, but biexponential behaviour for **DMA-BDP-1** and **DMA-BDP-2** (Table 2). The presence of short-lived and long-lived components in the dyads is consistent with excited-state CS dynamics. In line with previous studies, the shorter component is assigned to the rapid depopulation of the singlet excited state *via* CS state formation, while the longer component corresponds to residual fluorescence from the LE state.[40] To assess whether triplet excited states are populated *via* CS-mediated intersystem crossing (ISC), singlet oxygen quantum yield measurements were conducted. Despite the observed strong solvatochromism and charge transfer behavior, singlet oxygen quantum yields (Φ_Δ) for **DMA-BDP**s were low in all solvents tested. The highest Φ_Δ value of 9.1% was observed for **DMA-BDP-2** in ethyl acetate, indicating that ISC is inefficient in these systems.

Luminescence properties at 77 K

To confirm whether triplet excited states are formed in the studied compounds, we performed photoluminescence measurements at 77 K. This approach is commonly used for BODIPY derivatives, as their triplet states are poorly emissive at room temperature due to efficient non-radiative deactivation pathways.[41] To enhance ISC and facilitate detection of potential triplet emission, iodomethane was added as an external heavy-atom source. The photoluminescence spectra recorded at 77 K in frozen 2-MeTHF/iodomethane solutions showed only minor red-shift compared to room temperature spectra,

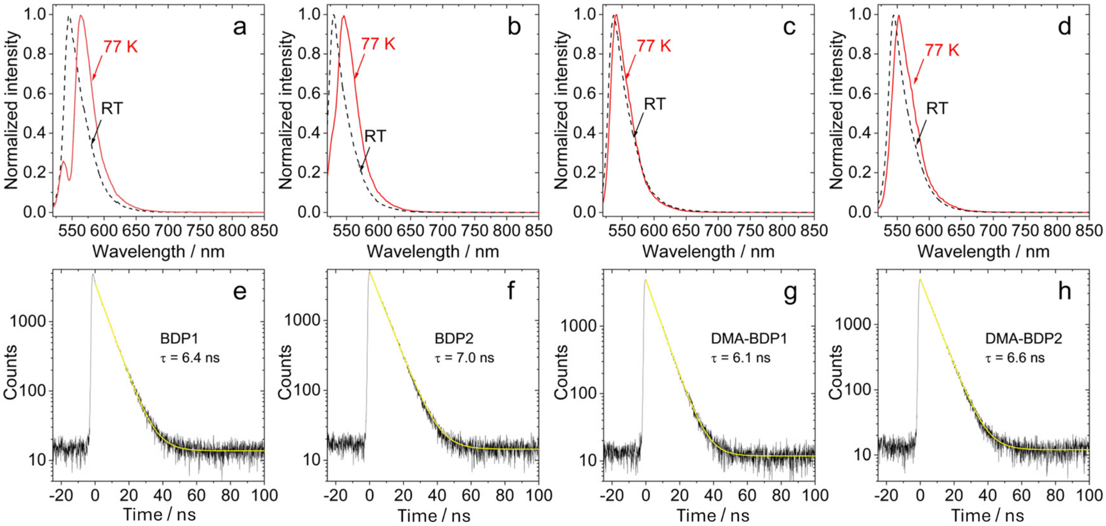

Fig. 4 Normalized emission spectra of (a) **BDP-1**, (b) **BDP-2**, (c) **DMA-BDP-1**, and (d) **DMA-BDP-2** recorded at room temperature and at 77 K (frozen 2-MeTHF/iodomethane solution, 1 : 2, v/v). Luminescence decay profiles at 77 K for (e) **BDP-1** at 560 nm, (f) **BDP-2** at 550 nm, (g) **DMA-BDP-1** at 530 nm, and (h) **DMA-BDP-2** at 550 nm. Excitation was performed using a 510 nm EPLED source. All measurements were carried out at a concentration of 1.0×10^{-4} M under degassed conditions.

without emergence of any new emissive bands (Fig. 4a–d). Typically, emission spectra at 77 K exhibit a hypsochromic shift due to the rigidity of the frozen matrix, which prevents solvent relaxation around the excited state. In contrast, the observed bathochromic shift suggests that in these dyads, the ground-state dipole moment may be sufficiently large to induce stabilization of the excited state even in frozen matrices. This behaviour is reminiscent of solvatochromic Reichardt's dyes, which also display unconventional temperature-dependent shifts due to pronounced ground-state polarity.[42] Taken together, the absence of any detectable phosphorescence at 77 K, even under heavy-atom conditions, indicates that ISC in these dyads is inefficient.

UV-Vis absorption spectra of radical anions and cations

To support the assignment of CS states in the transient absorption spectra of **DMA-BDP-1** and **DMA-BDP-2**, we investigated the UV-vis absorption spectra of their corresponding radical anions (Fig. 5). The radical anions were generated by chemical reduction using tetrabutylammonium hydroxide as the reductant, following established procedures.[43,44]

For **BDP-1**, which displays a reversible reduction wave (Fig. 5a), chemical reduction led to the appearance of new absorption features. The original absorption band at 528 nm decreased, while new bands emerged: a weak broad band in the 400–500 nm region and an intense band centred around 530 nm. These newly developed signals are consistent with the formation of **BDP-1** radical anions.[45] Similar spectral changes were observed for **BDP-2** (Fig. 5b), also consistent with its reversible reduction behaviour.

In contrast, for **DMA-BDP-1**, no absorption features were detected in the 400–500 nm region following reduction, which differs significantly from the parent **BDP-1**. This is attributed to the irreversible nature of the reduction process in **DMA-BDP-1** (Fig. 5c), suggesting that the radical anion is unstable under the conditions used and decomposes before a stable absorption spectrum can be recorded. **DMA-BDP-2** showed intermediate behaviour: the reduction was more reversible than in **DMA-BDP-1**, and its radical anion spectrum resembled that of **BDP-2.** However, the intensity of the band in the 400–500 nm range was significantly lower, indicating either lower stability or lower

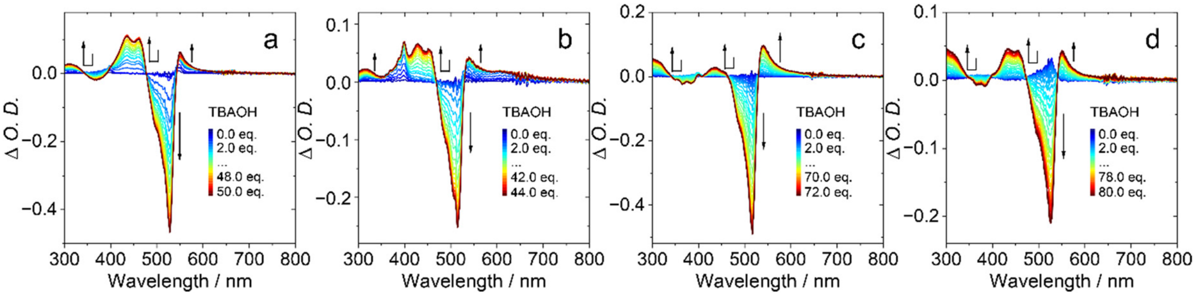

Fig. 5 Differential UV-vis absorption spectra of chemically reduced (a) **BDP-1**, (b) **BDP-2**, (c) **DMA-BDP-1**, and (d) **DMA-BDP-2** in deaerated DMF. The spectra show the evolution of $BDP^{-\bullet}$ radical anions obtained by subtracting the initial spectra (before TBAOH addition). Conditions: $c = 1.0 \times 10^{-5}$ M, $T = 20$ °C.

molar absorptivity of the radical species. To support the experimental observations, we also calculated the gas-phase absorption spectra of the radical anions (Fig. S30).

Femtosecond transient absorption spectroscopy

The excited-state dynamics of the two dyads, **DMA-BDP-1** and **DMA-BDP-2**, and the reference compounds **BDP-1** and **BDP-2** were studied using femtosecond transient absorption spectroscopy in the visible spectral range. For the dyads, two excitation wavelengths were tested: 490 nm, corresponding to the BODIPY absorption band, and 350 nm, which selectively excites the anthracene chromophore. The reference compounds were studied in toluene and DCM under 490 nm excitation. The data were analyzed using global analysis with a linear unidirectional decay model, enabling determination of the kinetic constants associated with the excited-state decay pathways and the corresponding evolution-associated difference spectra (EADS), which represent the distinct spectral components.

For reference compounds **BDP-1** and **BDP-2**, the EADS obtained from global analysis of the data recorded in toluene and DCM are shown in the SI (Fig. S15). The transient spectra and their evolution were found to be very similar in the two solvents. For both compounds, the transient absorption spectra feature an intense negative signal, attributed to a combination of ground-state bleaching (GSB) and stimulated emission (SE), along with a weak positive excited-state absorption (ESA) band in the 380–450 nm range. The transient spectra display limited spectral evolution, and the kinetic traces are well described using three decay components. The signal recorded immediately after excitation undergoes a slight decay on a 1–2 ps timescale, attributed to solvent-induced relaxation. This is followed by further evolution on a 30–40 ps timescale, during which the negative peak decreases in intensity, while the ESA band remains spectrally unchanged. This component is primarily associated with excited-state relaxation processes, including vibrational cooling and possible structural reorganization. The final EADS persists for approximately 4.3 ns in the case of **BDP-1** and 5.1 ns for **BDP-2**, in agreement with the high fluorescence quantum yields measured for both compounds, which are largely solvent-independent.

The transient spectra of the dyad **DMA-BDP-1** were recorded in three solvents of varying polarity: toluene, DCM and ACN. As expected from the measured fluorescence quantum yield values (Table 2), both the transient spectral features and the excited-state lifetimes are influenced by solvent polarity. In toluene, the transient spectra of **DMA-BDP-1** (Fig. 6) closely resemble those of the reference compound **BDP-1**. Immediately after excitation, an intense negative signal corresponding to GSB/SE and a weak positive ESA band are observed. The data are well fitted using four decay components. The transient signal gradually decreases in intensity over the probed time window, while maintaining the same spectral shape throughout. The fastest kinetic component corresponds to solvent-induced relaxation, followed by further excited-state relaxation processes with time constants of 19.5 ps and 93.7 ps. The 19.5 ps component primarily reflects vibrational cooling, while the longer component is likely associated with structural relaxation.

The excited-state lifetime is fitted as 4.7 ns, consistent with the high fluorescence quantum yield observed in this solvent. In more polar solvents, the spectral evolution differs significantly from that in toluene. In DCM, following an initial solvent relaxation component (0.8 ps), a substantial spectral transformation occurs within 8 ps, characterized by a pronounced decrease in the GSB/SE signal and the appearance of a positive

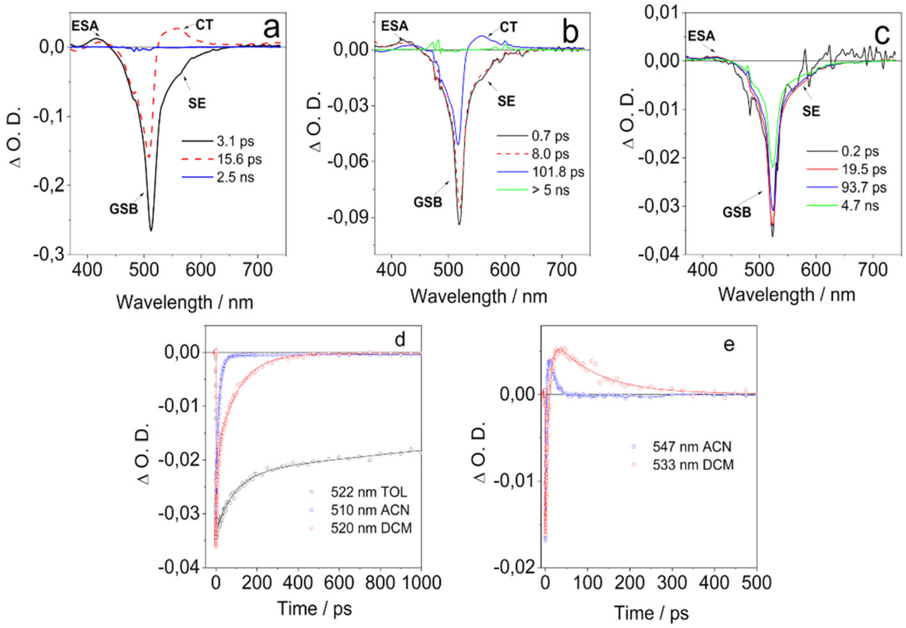

Fig. 6 EADS obtained from global analysis of the transient data recorded for **DMA-BDP-1** in (a) ACN, (b) DCM and (c) toluene upon excitation at 490 nm. Selected kinetic traces (d) and (e) in the three analyzed solvents upon excitation at 490 nm.

band centered around 550 nm. Based on the spectroelectrochemistry measurements presented in Fig. 5, and comparison with previous studies,[46] this evolution is attributed to photoinduced electron transfer, resulting in a CS state with the negative charge localized on the BODIPY unit and the positive charge on the anthracene. The CS state in DCM has a lifetime of ∼102 ps, after which charge recombination occurs. Only a weak residual signal is observed at later times.

A similar spectral evolution is observed in ACN, with the main difference being faster dynamics due to the higher polarity. Kinetic fitting indicates that in ACN, charge separation occurs in 3.1 ps and charge recombination in 15.6 ps. The solvent-dependent excited-state behavior is illustrated in Fig. 6, which compares the kinetic traces at the GSB peak across the three solvents (panel d) and the evolution of the CS marker band (panel e).

Measurements were repeated using excitation at 350 nm, selectively exciting the anthracene moiety. As was shown for previously studied BODIPY–anthracene dyads, excitation of the anthracene unit is followed by a fast (few ps) energy transfer to the BODIPY unit. Therefore, the results obtained under 350 nm excitation are very similar to those obtained upon BODIPY excitation (490 nm) in ACN and DCM, while some differences are observed in toluene (Fig. S16 and S17). In the more polar solvents, charge separation occurs on a timescale comparable to that previously observed: in ACN, the positive band associated with the CS state appears in 2.7 ps, while in DCM it forms in 7.8 ps. Under these excitation conditions, energy transfer from anthracene to BODIPY is also expected, but its timescale cannot be distinguished from that of CS. Charge recombination occurs within 15.4 ps in ACN and 128 ps in DCM. Notably, the residual signal observed after charge recombination is slightly more intense than that observed under 490 nm excitation in the same solvents.

In toluene, the dynamics differ somewhat from those observed upon direct BODIPY excitation. On the sub-picosecond timescale, an intense positive signal centred at ∼400 nm is observed and decays within ∼300 fs. Based on previous reports,[47] this signal is attributed to a fast solvent response, specifically a two-photon absorption signal from toluene. The subsequent EADS (Fig. S16c) shows the characteristic spectral profile of the BODIPY unit, with a strong GSB/SE band at 520 nm and a weak ESA band at 420 nm. The intensity of the GSB/SE band slightly increases over ∼23 ps, possibly due to energy transfer. On this same timescale, a weak positive band develops on the red side of the GSB, peaking at ∼600 nm, suggesting the occurrence of some degree of CS even in toluene. This positive signal decays in ∼597 ps, while the excited state persists longer, with a lifetime of ∼5.7 ns, primarily decaying *via* radiative processes.

The results obtained for **DMA-BDP-2** are very similar to those discussed for **DMA-BDP-1**. Charge separation and recombination (CS/CR) are observed upon excitation at 490 nm in both ACN and DCM, while no CS is detected in toluene (Fig. 7). The CS/CR kinetics are slightly slower compared to **DMA-BDP-1** and based on the intensity of the positive band centred at ∼565 nm, the efficiency of charge separation appears lower for **DMA-BDP-2** in DCM. In this sample, CS occurs in 8.8 ps in ACN (25.2 ps in DCM), while CR takes place within 22.3 ps in ACN and 204.9 ps in DCM.

Excitation at 350 nm yields similar results to those observed for **DMA-BDP-1**. The transient spectra and excited-state dynamics are comparable under both excitation conditions in ACN and DCM (Fig. S17 and S18). As with **DMA-BDP-1**, a small degree of CS is also observed in toluene when excited at 350 nm. A low-intensity, broad, positive band appears in the 600–700 nm region within 15.7 ps and decays within 505.6 ps.

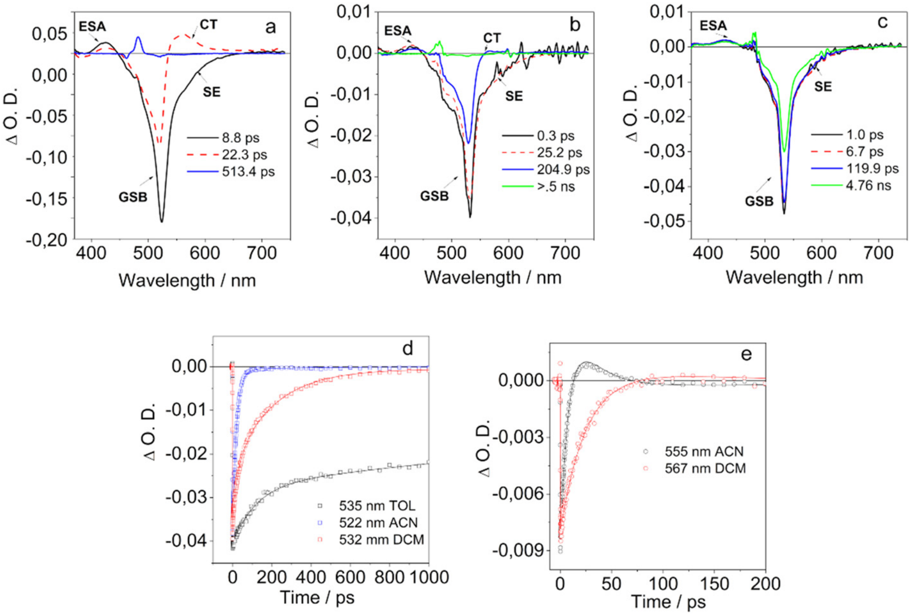

Fig. 7 EADS obtained from global analysis of the transient data recorded for **DMA-BDP-2** in (a) ACN, (b) DCM and (c) toluene upon excitation at 490 nm. Selected kinetic traces (d) and (e) in the three analyzed solvents.

The excited state persists for approximately 4.4 ns and primarily decays radiatively to the ground state.

Based on the estimated CS-state energies, the CS state is stabilized in more polar solvents, decreasing from *ca.* 2.08 eV in DCM to 1.95 eV in ACN for **DMA-BDP-1**, and from 2.04 eV to 1.96 eV for **DMA-BDP-2** (Table 1). At the same time, the measured charge-recombination lifetimes become substantially shorter in ACN than in DCM. This trend indicates that lowering the energy of the CS state accelerates recombination, which is qualitatively consistent with charge recombination occurring in the Marcus normal regime.

Nanosecond time-resolved transient absorption spectroscopy

Although low singlet oxygen quantum yields were observed, this does not rule the possibility that ISC occurs in these dyads; inefficient singlet oxygen generation may also result from short triplet state lifetimes (*e.g.*, $\tau_T < 0.1$ μs) or poor energy transfer efficiency. Triplet formation remains possible *via* mechanisms such as the $S_1 \rightarrow T_2$ pathway, as reported for asymmetrically substituted BODIPY.[35]

To clarify the situation, since no transient signal was observed for the compounds alone, we employed an intermolecular photosensitization strategy to populate the triplet state of the compounds. Based on TDDFT calculations, the energy of the T_1 state in the BODIPY-based dyads was estimated to be approximately 1.50 eV. Therefore, anthracene (**An**), which has a higher-lying T_1 state ($\sim$1.8 eV), was selected as the triplet sensitizer.[48]

Upon selective excitation of anthracene in a degassed DMF solution containing **BDP-1** (Fig. 8a) using a 355 nm nanosecond laser pulse, a strong transient absorption band centred at 430 nm appeared, attributed to excited-state absorption (ESA) of the **An** triplet state.[49] Simultaneously, a ground-state bleaching (GSB) signal at 530 nm was observed, corresponding to the depletion of the **BDP-1** ground state. No transient signals were detected for **BDP-1** alone under the same conditions, confirming that the observed signal arises from intermolecular triplet–triplet energy transfer (TTET) between **An** and **BDP-1**.

To dissect the evolution of transient species, global analysis was applied to the ns-TA data (Fig. 9b). Two species were resolved: the first corresponds to the T_1 state of anthracene (TTET donor), and the second to the T_1 state of **BDP-1**. Under the applied conditions, the TTET time constant was determined to be 25.7 μs, and the lifetime of the **BDP-1** triplet state was estimated to be 84.5 μs.

Similar experiments for **BDP-2** (Fig. S20) yielded a triplet state lifetime of 50.2 μs. It should be noted that these values are influenced by triplet–triplet annihilation (TTA), which depends on laser fluence and compound concentration. Similar experiments were performed for **DMA-BDP-1** and **DMA-BDP-2** (Fig. 9 and S21). For **DMA-BDP-1**, the ns-TA spectra of the **An**/**DMA-BDP-1** mixture closely resembled those of the **An**/**BDP-1** system. Global analysis revealed two transient species: the first was assigned to the anthracene triplet, and the second to the ^{3}LE state of **DMA-BDP-1**. Notably, the triplet spin density was localized on the BODIPY moiety, suggesting the absence of a ^{3}CT or ^{3}CS character. In contrast, attempts to perform TTET experiments in polar solvents such as acetonitrile failed to generate any detectable signal coming from the triplet state of the dyads.

To confirm the nature of the triplet states, DFT computations were carried out to visualize the electron spin density surfaces of **DMA-BDP-1** and **DMA-BDP-2** (Fig. S31 and S32). In both polar and nonpolar solvent models, the unpaired electron density was confined to the BODIPY core, consistent with a localized ^{3}LE state rather than a charge-transfer ^{3}CT state. These computational results fully support the spectroscopic data and the energy-level analysis of the CS *vs.* LE states. The photophysical processes of **DMA-BDP-1** and **DMA-BDP-2** upon photoexcitation are summarized in Scheme 2 and Scheme S1. In non-polar solvents such as hexane, photoinduced intramolecular electron transfer is thermodynamically unfavourable. As a result, the fluorescence of **DMA-BDP-1** closely resembles that of the parent chromophore **BDP-1**, with no significant quenching observed. In contrast, in polar solvents such as acetonitrile, the CS state is stabilized and lies approximately 0.4 eV below the first singlet excited state (^{1}LE) of the chromophore. This energy difference favours photoinduced electron transfer, leading to efficient fluorescence quenching.

Despite the formation of the CS state in polar solvents, no long-lived charge-separated species are detected in femtosecond (fs-TA) or nanosecond transient absorption (ns-TA) spectra. In all solvents studied, the CS state remains energetically higher than the lowest triplet state (T_1), which is localized on the BODIPY core. Although higher triplet states (T_2 or T_3) may lie close in

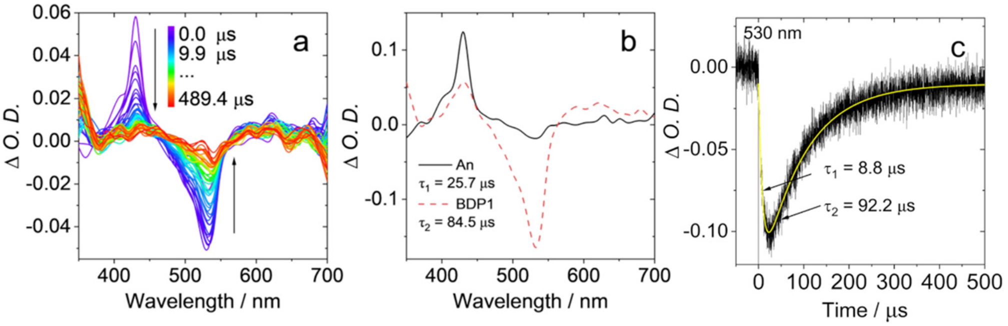

Fig. 8 (a) The ns-TA spectra recorded for the mixture of **BDP-1** ($c = 1.0 \times 10^{-5}$ M) and **An** ($c = 5.0 \times 10^{-6}$ M) after pulsed laser excitation at 355 nm in deaerated toluene. (b) Evolution-associated difference spectra (EADS) based on the data presented in (a). (c) Decay trace of the mixture of **BDP-1** and **An** at 530 nm.

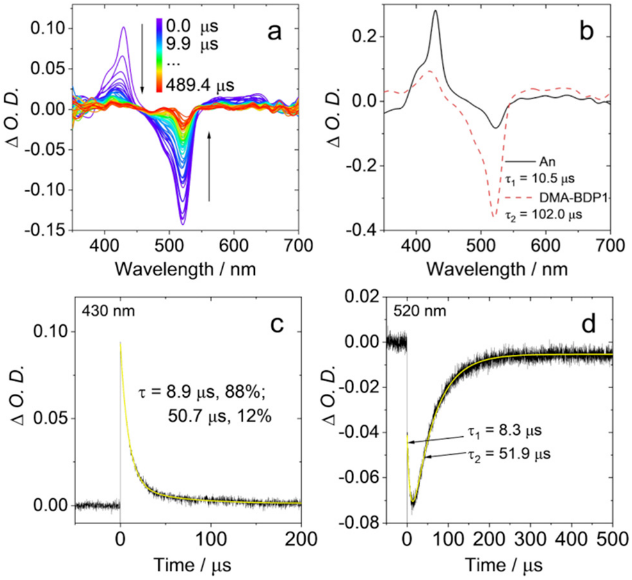

Fig. 9 (a) Nanosecond transient absorption (ns-TA) spectra of a deaerated toluene solution containing **DMA-BDP-1** (c = 1.0 × 10^{-5} M) and anthracene (c = 5.0 × 10^{-6} M) recorded after 355 nm pulsed laser excitation. (b) Evolution-associated difference spectra (EADS) obtained from global analysis of data in (a). (c) Kinetic trace at 430 nm, corresponding to the triplet state of anthracene. (d) Kinetic trace at 520 nm, corresponding to the triplet state of **DMA-BDP-1**.

energy to the ^{1}CS states, no efficient ISC is observed. This suggests that the CS state recombination outcompetes intersystem crossing (ISC) in the studied systems.

Conclusions

Although SOCT-ISC is traditionally associated with orthogonal D–A arrangements, recent studies have demonstrated triplet formation in non-orthogonal systems, such as facially stacked dye dimers,[50] polymers[51] and supramolecular assemblies.[52] In such cases, the radical-pair intersystem crossing (RP-ISC) pathway[53] has been invoked, but again, experimental evidence of this mechanism remains limited due to a lack of model systems. In this study, we designed and synthesized a series of rigid donor–acceptor dyads in which anthracene and BODIPY chromophores are connected *via* a fused bicyclo[2.2.2]octane spacer. This structural motif enforces a fixed, non-orthogonal geometry between donor and acceptor units, suppressing the conformational flexibility typical for previously studied BODIPY-based D–A dyads. DMA-BDP dyads represent a new type of donor–acceptor system with a well-defined spatial arrangement and strong through-bond coupling. Single-crystal X-ray analysis confirmed the constrained geometry and minimal torsional distortion across the series, validating the use of this spacer for enforcing structural rigidity.

Optical spectroscopy and femtosecond transient absorption experiments revealed that despite the rigidity and steric bulk of the spacer, photoinduced charge separation in polar solvents remains efficient, occurring on a 2–9 ps timescale, comparable to that of more flexible analogues. However, a key finding is that no efficient triplet state formation was observed (Φ_Δ < 10%), even under conditions that favour SOCT-ISC. Neither phosphorescence nor ^{3}CS intermediates were detected, including at low temperatures or in the presence of external heavy atoms. These results indicate that the rigid D–A geometry successfully blocks ISC from the charge-separated state by preventing the conformational reorganization required for efficient spin–orbit coupling.

This outcome is particularly relevant for systems where triplet formation is detrimental, such as in fluorescence-based sensors, organic photovoltaics, and molecular electronics, where CS state decay into triplets typically constitutes an energy loss channel. The ability to suppress ISC by using the

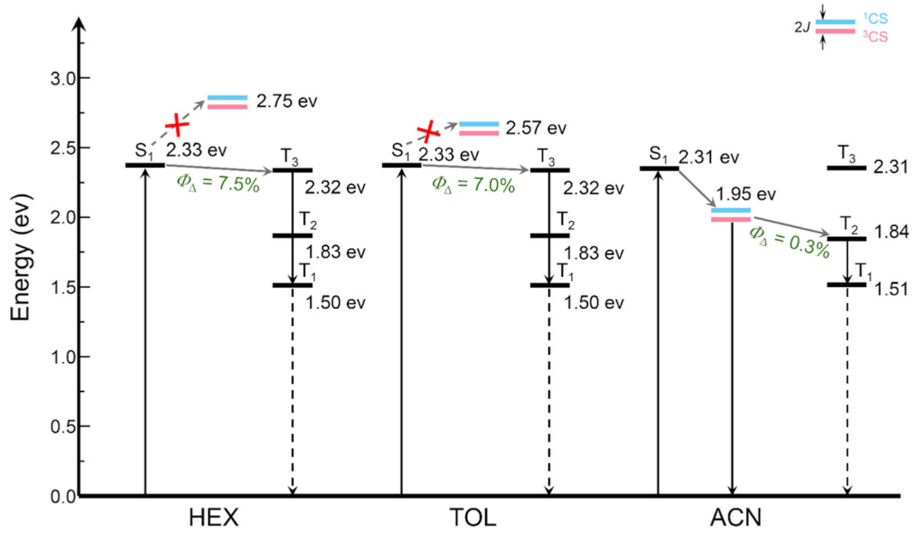

Scheme 2 Photophysical processes of **DMA-BDP-1** in different solvents. Excited-state energies were calculated by TDDFT at the B3LYP/6-31G(d) level using Gaussian 16. Charge-transfer (CT) state energies were estimated from electrochemical data.

bicyclo[2.2.2]octane spacer offers a new design strategy for such applications.

Our study further reveals that, contrary to prevailing assumptions in the field, the rigid geometry did not lead to extended CS state lifetimes. Instead, the CT states remained short-lived (15–205 ps), undergoing fast recombination. This directly challenges the commonly held view that rigidity in D–A systems correlates with longer-lived CS states. Our results suggest that rigidity alone is insufficient for lifetime extension, and that other factors, possibly electronic structure or energy-level alignment, are responsible for long-lived CS states reported in other systems. This hypothesis warrants further investigation.

Author contributions

M. D. performed optical measurements, analyzed the data, and contributed to manuscript writing. Y. Wu carried out nanosecond transient and electrochemical measurements. G. S. performed ultrafast transient absorption experiments. C. N. synthesized the BODIPY compounds. B. T. obtained X-ray crystallographic data and conducted the analysis with assistance from M. O. S. J. Z. analyzed the data and contributed to manuscript writing. M. D. D. analyzed the ultrafast transient absorption data and contributed to manuscript writing. M. F. conceived the project, synthesized key precursors, and coordinated manuscript preparation. All authors discussed the results and approved the final version of the manuscript.

Conflicts of interest

There are no conflicts to declare.

Data availability

The data supporting this article have been included as part of the supplementary information (SI). Supplementary information: synthesis and characterization, photophysical data, transient electronic absorption data, X-ray diffraction, and computational details. See DOI: https://doi.org/10.1039/d6tc00131a.

CCDC 2517531 and 2517532 contain the supplementary crystallographic data for this paper.[54a,b]

Acknowledgements

The authors acknowledge Research Ireland award 21/FFP-A/9214 (DyeSICPhoto) for supporting this work. M. D. D. acknowledges support from the European Union's Next Generation EU Program with the I-PHOQS Infrastructure [No. IR0000016, ID D2B8D520, and CUP B53C22001750006] ''Integrated infrastructure initiative in Photonic and Quantum Sciences.''

Notes and references

1 (*a*) D. Gust, T. A. Moore and A. L. Moore, *Acc. Chem. Res.*, 2009, **42**, 1890–1898; (*b*) M. R. Wasielewski, *Acc. Chem. Res.*, 2009, **42**, 1910–1921; (*c*) S. Fukuzumi, K. Ohkubo and T. Suenobu, *Acc. Chem. Res.*, 2014, **47**, 1455–1464; (*d*) F. D'Souza and O. Ito, *Chem. Soc. Rev.*, 2012, **41**, 86–96.

2 D. R. Whang and D. H. Apaydin, *ChemPhotoChem*, 2018, **2**, 148.

3 S. Fukuzumi and K. Ohkubo, *Org. Biomol. Chem.*, 2014, **12**, 6059–6071.

4 (*a*) E. Allard, J. Cousseau, J. Orduña, J. Garín, H. Luo, Y. Araki and O. Ito, *Phys. Chem. Chem. Phys.*, 2002, **4**, 5944–5951; (*b*) H. Lin, Q.-B. Lv, H.-F. Wang, K.-Q. Zhao, P. Hu, B.-Q. Wang, B. Heinrich and B. Donnio, *Dyes Pigm.*, 2022, **197**, 109911; (*c*) Y. H. Geerts, O. Debever, C. Amato and S. Sergeyev, *Beilstein J. Org. Chem.*, 2009, **5**, 49; (*d*) T. L. Easun, W. Z. Alsindi, M. Towrie, K. L. Ronayne, X.-Z. Sun, M. D. Ward and M. W. George, *Inorg. Chem.*, 2008, **47**, 5071–5078; (*e*) H. Wu, D. Zhang, L. Su, K. Ohkubo, C. Zhang, S. Yin, L. Mao, Z. Shuai, S. Fukuzumi and D. Zhu, *J. Am. Chem. Soc.*, 2007, **129**, 6839–6846; (*f*) J. Baffreau, S. Leroy-Lhez, N. Vân Anh, R. Williams and P. Hudhomme, *Chem. – Eur. J.*, 2008, **14**, 4974–4992.

5 (*a*) D. M. Guldi, M. Maggini, G. Scorrano and M. Prato, *J. Am. Chem. Soc.*, 1997, **119**, 974–980; (*b*) S. R. Greenfield, W. A. Svec, D. Gosztola and M. R. Wasielewski, *J. Am. Chem. Soc.*, 1996, **118**, 6767–6777; (*c*) A. C. Benniston, G. Copley, K. J. Elliott, R. W. Harrington and W. Clegg, *Eur. J. Org. Chem.*, 2008, 2705–2713; (*d*) P. Kölle, I. Pugliesi, H. Langhals, R. Wilcken, A. J. Esterbauer, R. de Vivie-Riedle and E. Riedle, *Phys. Chem. Chem. Phys.*, 2015, **17**, 25061–25072; (*e*) A. Osuka, H. Yamada, K. Maruyama, N. Mataga, T. Asahi, M. Ohkouchi, T. Okada, I. Yamazaki and Y. Nishimura, *J. Am. Chem. Soc.*, 1993, **115**, 9439–9452; (*f*) H. Kanato, K. Takimiya, T. Otsubo, Y. Aso, T. Nakamura, Y. Araki and O. Ito, *J. Org. Chem.*, 2004, **69**, 7183–7189.

6 (*a*) R. Fong, D. I. Schuster and S. R. Wilson, *Org. Lett.*, 1999, **1**, 729–732; (*b*) L.-P. Zhang, B. Chen, L.-Z. Wu, C.-H. Tung, H. Cao and Y. Tanimoto, *Chem. – Eur. J.*, 2003, **9**, 2763–2769; (*c*) M. Braga and S. Larsson, *J. Phys. Chem.*, 1993, **97**, 8929–8936; (*d*) S. MacMahon, R. Fong, P. S. Baran, I. Safonov, S. R. Wilson and D. I. Schuster, *J. Org. Chem.*, 2001, **66**, 5449–5455.

7 (*a*) H. Hokari, U. Akiba and M. Fujihira, *J. Chem. Soc., Chem. Commun.*, 1995, 2139–2140; (*b*) T. J. Chow, N.-R. Chiu, H.-C. Chen, C.-Y. Chen, W.-S. Yu, Y.-M. Cheng, C.-C. Cheng, C.-P. Chang and P.-T. Chou, *Tetrahedron*, 2003, **59**, 5719–5730; (*c*) G. M. Locke, S. S. R. Bernhard and M. O. Senge, *Chem. – Eur. J.*, 2019, **25**, 4590; (*d*) Y. J. Yun, F. Peccati, G. P. Wiederrecht, D. J. Gosztola, B. T. Diroll, G. Jiménez-Osés and A. Jean-Luc Ayitou, *J. Mater. Chem. C*, 2022, **10**, 7093–7102.

8 B. Albinsson and J. Mårtensson, *J. Photochem. Photobiol., C*, 2008, **9**, 138–155.

9 Z. R. Grabowski, K. Rotkiewicz and W. Rettig, *Chem. Rev.*, 2003, **103**, 3899.

10 P. F. H. Schwab, M. D. Levin and J. Michl, *Chem. Rev.*, 1999, **99**, 1863.

11 (*a*) P. T. Gulyas, S. J. Langford, N. R. Lokan, M. G. Ranasinghe and M. N. Paddon-Row, *J. Org. Chem.*, 1997,

62, 3038; (*b*) T. Könekamp, A. Ruiz, J. Duwenhorst, W. Schmidt, T. Borrmann, W.-D. Stohrer and F.-P. Montforts, *Chem. – Eur. J.*, 2007, **13**, 6595–6604; (*c*) K.-Y. Chen, C.-C. Hsieh, Y.-M. Cheng, C.-H. Lai, P.-T. Chou and T. J. Chow, *J. Phys. Chem. A*, 2006, **110**, 12136–12144.

12 (*a*) K. B. Daisymol and K. R. Gopidas, *J. Phys. Chem. Lett.*, 2023, **14**, 977; (*b*) K. B. Daisymol and K. R. Gopidas, *J. Mol. Struct.*, 2024, **1312**, 138456.

13 Y. J. Yun, N. Kamatham, M. K. Manna, J. Li, S. Liu, G. P. Wiederrecht, D. J. Gosztola, B. T. Diroll, A. Y. Rogachev and A. Jean-Luc Ayitou, *J. Phys. Chem. C*, 2020, **124**, 12205.

14 A. D. Joran, B. A. Leland, G. G. Geller, J. J. Hopfield and P. B. Dervan, *J. Am. Chem. Soc.*, 1984, **106**, 6090.

15 R. H. Goldsmith, J. Vura-Weis, A. M. Scott, S. Borkar, A. Sen, M. A. Ratner and M. R. Wasielewski, *J. Am. Chem. Soc.*, 2008, **130**, 7659–7669.

16 (*a*) H. E. Zimmerman and D. R. McKelvey, *J. Am. Chem. Soc.*, 1971, **93**, 3653; (*b*) N. Lokan, M. N. Paddon-Row, T. A. Smith, M. La Rosa, K. P. Ghiggino and S. Speiser, *J. Am. Chem. Soc.*, 1999, **121**, 2917–2918; (*c*) T. A. Smith, N. Lokan, N. Cabral, S. R. Davies, M. N. Paddon-Row and K. P. Ghiggino, *J. Photochem. Photobiol., A*, 2002, **149**, 55–69.

17 (*a*) J. W. Verhoeven, H. J. van Ramesdonk, M. M. Groeneveld, A. C. Benniston and A. Harriman, *ChemPhysChem*, 2005, **6**, 2251–2260; (*b*) A. Karimata, H. Kawauchi, S. Suzuki, M. Kozaki, N. Ikeda, K. Keyaki, K. Nozaki, K. Akiyama and K. Okada, *Chem. Lett.*, 2013, **42**, 794–796; (*c*) X. Chen, A. A. Sukhanov, Y. Yan, D. Bese, C. Bese, J. Zhao, V. K. Voronkova, A. Barbon and H. G. Yaglioglu, *Angew. Chem., Int. Ed.*, 2022, **61**, e202203758 (*Angew. Chem.*, 2022, **134**, e202203758); (*d*) H. Wang, A. A. Sukhanov, A. Iagatti, L. Bussotti, X. Zhao, J. Zhao, V. K. Voronkova and M. Di Donato, *Chem. – Eur. J.*, 2023, **29**, e202301125.

18 Z. E. X. Dance, Q. Mi, D. W. McCamant, M. J. Ahrens, M. A. Ratner and M. R. Wasielewski, *J. Phys. Chem. B*, 2006, **110**, 25163–25173.

19 (*a*) M. A. Filatov, *Org. Biomol. Chem.*, 2020, **18**, 10; (*b*) X. Zhang, Z. Wang, Y. Hou, Y. Yan, J. Zhao and B. Dick, *J. Mater. Chem. C*, 2021, **9**, 11944.

20 (*a*) Z. E. X. Dance, S. M. Mickley, T. M. Wilson, A. B. Ricks, A. M. Scott, M. A. Ratner and M. R. Wasielewski, *J. Phys. Chem. A*, 2008, **112**, 4194–4201; (*b*) M. T. Colvin, A. B. Ricks, A. M. Scott, D. T. Co and M. R. Wasielewski, *J. Phys. Chem. A*, 2012, **116**, 1923–1930.

21 H. Oevering, M. N. Paddon-Row, M. Heppener, A. M. Oliver, E. Cotsaris, J. W. Verhoeven and N. S. Hush, *J. Am. Chem. Soc.*, 1987, **109**, 3258–3269.

22 K. Y. Chen, T. C. Chang and M. Y. Yeh, *Tetrahedron Lett.*, 2002, **43**, 8115–8119.

23 (*a*) M. A. Filatov, S. Karuthedath, P. M. Polestshuk, H. Savoie, K. J. Flanagan, C. Sy, E. Sitte, M. Telitchko, F. Laquai, R. W. Boyle and M. O. Senge, *J. Am. Chem. Soc.*, 2017, **139**, 6282; (*b*) Z. Wang and J. Zhao, *Org. Lett.*, 2017, **19**, 4492; (*c*) J. T. Buck, A. M. Boudreau, A. DeCarmine, R. W. Wilson, J. Hampsey and T. Mani, *Chem*, 2018, **5**, 1; (*d*) N. Kiseleva, M. A. Filatov, M. Oldenburg, D. Busko, M. Jakoby, I. A. Howard, B. S. Richards, M. O. Senge, S. M. Borisov and A. Turshatov, *Chem. Commun.*, 2018, **54**, 1607–1610.

24 M. A. Filatov, S. Karuthedath, P. M. Polestshuk, S. Callaghan, K. J. Flanagan, M. Telitchko, T. Wiesner, F. Laquai and M. O. Senge, *Phys. Chem. Chem. Phys.*, 2018, **20**, 8016.

25 Y. Hu, Y. Hou, Z. Wang, Y. Li and J. Zhao, *J. Chem. Phys.*, 2020, **153**, 224304.

26 T. Mikulchyk, S. Karuthedath, C. S. P. De Castro, A. A. Buglak, A. Sheehan, A. Wieder, F. Laquai, I. Naydenova and M. A. Filatov, *J. Mater. Chem. C*, 2022, **10**, 11588.

27 T. Okujima, Y. Tomimori, J. Nakamura, H. Yamada, H. Uno and N. Ono, *Tetrahedron*, 2010, **66**, 6895–6900.

28 M. A. Filatov, T. Mikulchyk, M. Hodée, M. Dvoracek, V. N. K. Mamillapalli, A. Sheehan, C. Newman, S. M. Borisov, D. Escudero and I. Naydenova, *J. Mater. Chem. C*, 2025, **13**, 6993–7003.

29 M. A. Filatov, F. Etzold, D. Gehrig, F. Laquai, D. Busko, K. Landfester and S. Baluschev, *Dalton Trans.*, 2015, **44**, 19207–19217.

30 A. Sheehan, T. Mikulchyk, C. S. P. De Castro, S. Karuthedath, W. Althobaiti, M. Dvoracek, Sabad-e-Gul, H. J. Byrne, F. Laquai, I. Naydenova and M. A. Filatov, *J. Mater. Chem. C*, 2023, **11**, 15084–15096.

31 (*a*) Bruker, *APEX3 V2017.3-0*, Bruker AXS Inc., Madison, Wisconsin, (USA), 2017; (*b*) Bruker, *SAINT, v8.37A*, Bruker AXS Inc., Madison, Wisconsin, USA, 2015; (*c*) L. Krause, R. Herbst-Irmer, G. M. Sheldrick and D. Stalke, *J. Appl. Crystallogr.*, 2015, **48**, 3–10; (*d*) G. M. Sheldrick, *Acta Crystallogr.*, 2015, **A71**, 3–8; (*e*) G. M. Sheldrick, *Acta Crystallogr.*, 2015, **C71**, 3–8; (*f*) O. V. Dolomanov, L. J. Bourhis, R. J. Gildea, J. A. K. Howard and H. Puschmann, *J. Appl. Crystallogr.*, 2009, **42**, 339–341.

32 M. Dvoracek, C. Newman, M. Drobizhev, B. Twamley, M. O. Senge, S. A. Vinogradov and M. A. Filatov, *J. Org. Chem.*, 2025, **90**, 12984–12997.

33 M. J. Frisch, G. W. Trucks, H. B. Schlegel, G. E. Scuseria, M. A. Robb, J. R. Cheeseman, G. Scalmani, V. Barone, G. A. Petersson, H. Nakatsuji, X. Li, M. Caricato, A. V. Marenich, J. Bloino, B. G. Janesko, R. Gomperts, B. Mennucci, H. P. Hratchian, J. V. Ortiz, A. F. Izmaylov, J. L. Sonnenberg, D. Williams-Young, F. Ding, F. Lipparini, F. Egidi, J. Goings, B. Peng, A. Petrone, T. Henderson, D. Ranasinghe, V. G. Zakrzewski, J. Gao, N. Rega, G. Zheng, W. Liang, M. Hada, M. Ehara, K. Toyota, R. Fukuda, J. Hasegawa, M. Ishida, T. Nakajima, Y. Honda, O. Kitao, H. Nakai, T. Vreven, K. Throssell, J. A. Montgomery, Jr., J. E. Peralta, F. Ogliaro, M. J. Bearpark, J. J. Heyd, E. N. Brothers, K. N. Kudin, V. N. Staroverov, T. A. Keith, R. Kobayashi, J. Normand, K. Raghavachari, A. P. Rendell, J. C. Burant, S. S. Iyengar, J. Tomasi, M. Cossi, J. M. Millam, M. Klene, C. Adamo, R. Cammi, J. W. Ochterski, R. L. Martin, K. Morokuma, O. Farkas, J. B. Foresman and D. J. Fox, *Gaussian 16, Revision B.01*, Gaussian, Inc., Wallingford CT, 2016.

34 A. B. Nepomnyashchii, S. Cho, P. J. Rossky and A. J. Bard, *J. Am. Chem. Soc.*, 2010, **132**, 17550–17559.

35 R. Ziessel, B. Allen, D. Rewinska and A. Harriman, *Chem. – Eur. J.*, 2009, **15**, 7382–7393.

36 R. F. Kubin and A. N. Fletcher, *J. Lumin.*, 1982, **27**, 455–462.

37 Y. Zhao, R. Duan, J. Zhao and C. Li, *Chem. Commun.*, 2018, **54**, 12329–12332.

38 N. Kiseleva, D. Busko, B. S. Richards, M. A. Filatov and A. Turshatov, *J. Phys. Chem. Lett.*, 2020, **11**, 6560–6566.

39 S. Mukherjee and P. Thilagar, *RSC Adv.*, 2015, **5**, 2706.

40 X. Chen, N. Rehmat, I. V. Kurganskii, P. Maity, A. Elmali, J. Zhao, A. Karatay, O. F. Mohammed and M. V. Fedin, *Chem. – Eur. J.*, 2023, **29**, e202302137.

41 X.-F. Zhang, X. Yang, K. Niu and H. Geng, *J. Photochem. Photobiol., A*, 2014, **285**, 16–20.

42 K. Echelberry, H. Burda, P. Willis, W. W. Parson and C. Burda, *J. Chem. Phys.*, 2023, **159**, 154506.

43 X. Chen, I. V. Kurganskii, Z. Zhuang, Y. He, N. Rehmat, Z. Mahmood, J. Zhao, M. V. Fedin, L. Luo, D. Escudero and B. Dick, *Angew. Chem., Int. Ed.*, 2025, **64**, e202500718.

44 F. S. Goodson, D. K. Panda, S. Ray, A. Mitra, S. Guha and S. Saha, *Org. Biomol. Chem.*, 2013, **11**, 4797–4803.

45 Y. Hou, I. Kurganskii, A. Elmali, H. Zhang, Y. Gao, L. Lv, J. Zhao, A. Karatay, L. Luo and M. Fedin, *J. Chem. Phys.*, 2020, **152**, 114701.

46 (*a*) M. A. Filatov, S. Karuthedath, P. M. Polestshuk, S. Callaghan, K. J. Flanagan, T. Wiesner, F. Laquai and M. O. Senge, *ChemPhotoChem*, 2018, **2**, 606; (*b*) Y. Wu, M. M. Bakirov, A. A. Sukhanov, H. Cao, J. Li, S. Liao, J. Zhao, Y. E. Kandrashkin, V. K. Voronkova and M.-D. Li, *Phys. Chem. Chem. Phys.*, 2025, **27**, 20013–20022; (*c*) P. Gautam, R. Misra, M. B. Thomas and F. D'Souza, *Chem. – Eur. J.*, 2017, **23**, 9192; (*d*) A. Karatay, H. Yilmaz, E. A. Yildiz, G. Sevinc, M. Hayvali, B. Boyacioglu, H. Unvere and A. Elmalia, *Phys. Chem. Chem. Phys.*, 2022, **24**, 25495.

47 S.-H. Gong and A. Penzkofer, *Opt. Quantum Electron.*, 1999, **31**, 1145–1170.

48 (*a*) X. Zhang, A. A. Sukhanov, X. Liu, M. Taddei, J. Zhao, A. Harriman, V. K. Voronkova, Y. Wan, B. Dick and M. Di Donato, *Chem. Sci.*, 2023, **14**, 5014–5027; (*b*) X. Chen, A. A. Sukhanov, M. Taddei, B. Dick, J. Zhao, V. K. Voronkova and M. Di Donato, *J. Phys. Chem. Lett.*, 2022, **13**, 8740–8748; (*c*) K. Chen, M. Hussain, S. S. Razi, Y. Hou, E. A. Yildiz, J. Zhao, H. G. Yaglioglu and M. Di Donato, *Inorg. Chem.*, 2020, **59**, 14731–14745.

49 (*a*) Y. Hou, T. Biskup, S. Rein, Z. Wang, L. Bussotti, N. Russo, P. Foggi, J. Zhao, M. Di Donato, G. Mazzone and S. Weber, *J. Phys. Chem. C*, 2018, **122**, 27850–27865; (*b*) Y. Hou, T. Biskup, S. Rein, Z. Wang, L. Bussotti, N. Russo, P. Foggi, J. Zhao, M. Di Donato, G. Mazzone and S. Weber, *J. Phys. Chem. C*, 2018, **122**, 27850–27865.

50 (*a*) D. Veldman, S. M. A. Chopin, S. C. J. Meskers, M. M. Groeneveld, R. M. Williams and R. A. J. Janssen, *J. Phys. Chem. A*, 2008, **112**, 5846–5857; (*b*) K. M. Lefler, K. E. Brown, W. A. Salamant, S. M. Dyar, K. E. Knowles and M. R. Wasielewski, *J. Phys. Chem. A*, 2013, **117**, 10333–10345; (*c*) P. Spenst, R. M. Young, M. R. Wasielewski and F. Würthner, *Chem. Sci.*, 2016, **7**, 5428–5434.

51 A. A. Cullen, A. Rajagopal, K. Heintz, A. Heise, R. Murphy, I. V. Sazanovich, G. M. Greetham, M. Towrie, C. Long, D. Fitzgerald-Hughes and M. T. Pryce, *J. Phys. Chem. B*, 2021, **125**, 1550–1557.

52 R. Sánchez-Naya and F. Beuerle, *Angew. Chem., Int. Ed.*, 2025, **64**, e202423676.

53 C. D. Buckley, D. A. Hunter, P. J. Hore and K. A. McLauchlan, *Chem. Phys. Lett.*, 1987, **135**, 307–312.

54 (*a*) CCDC 2517531: Experimental Crystal Structure Determination, 2026, DOI: 10.5517/ccdc.csd.cc2qhppm; (*b*) CCDC 2517532: Experimental Crystal Structure Determination, 2026, DOI: 10.5517/ccdc.csd.cc2qhpqn.